PHOTOPRODUCTION OF $\pi°$ MESONS FROM NEUTRONS IN THE ENERGY REGION FROM 500 TO 900 MeV*

By

Yasuo HEMMI

Department of Physics, Fuculty of Science, Kyoto University, Kyoto, Japan

(*Received January 16, 1971*)

ABSTRACT

The present paper reports the experimental results on the ratio, $R_{00}=[d\sigma/d\Omega\,(\gamma n\to\pi°n)]/[d\sigma/d\Omega\,(\gamma p\to\pi°p)]$, at the c.m. pion angles of 60°, 90°, 105°, 120° and 140° in the energy region of the incident photon between 500 and 900 MeV. The measurement has been performed by using a liquid deuterium target. The $\pi°$ mesons and the recoiled nucleons were detected by a pair of Cherenkov counters combined with the lead spark chambers and plastic scintillation counters consisting of 16 modules, respectively.

The experimental results are compared with the results of the recent phenomenological analyses.

1. Introduction

The investigation of the single pion photoproduction provide the valuable information on the pion-nucleon interaction and the electromagnetic interaction of the photon with the nucleon.

Nowadays, considerable amounts of the experimental informations have been accumulated on the single pion photoproduction from protons,

$$\gamma+p\to\pi^{+}+n, \qquad (1\text{-}1)$$

$$\gamma+p\to\pi^{0}+p, \qquad (1\text{-}2)$$

with energies below 1.5 GeV.

Recently, the experimental studies in the π^- photoproduction from neutrons,

$$\gamma+n\to\pi^{-}+p, \qquad (1\text{-}3)$$

have been performed extensively.[2]

However, the photoproduction of neutral pions from neutrons,

$$\gamma+n\to\pi°+n, \qquad (1\text{-}4)$$

has been scarecely investigated because of the difficulty of the experiment.[3]

In the single pion photoproduction from nucleons, the photoproduction amplitude of pions can be expressed with a sum of the isoscalar and isovector amplitudes following the isospin decomposition as follows ;[4]

---

*) A part of this paper was published in Physics Letters.[1]

$$T^{+} = \sqrt{2}\left(T^{(0)} + \frac{1}{3}T^{(1/2)} - \frac{1}{3}T^{(3/2)}\right), \tag{1-5}$$

$$T^{0} = T^{(0)} + \frac{1}{3}T^{(1/2)} + \frac{2}{3}T^{(3/2)}, \tag{1-6}$$

$$T^{-} = \sqrt{2}\left(T^{(0)} - \frac{1}{3}T^{(1/2)} + \frac{1}{3}T^{(3/2)}\right), \tag{1-7}$$

$$T^{n0} = -\left(T^{(0)} - \frac{1}{3}T^{(1/2)} - \frac{2}{3}T^{(3/2)}\right), \tag{1-8}$$

where T^{+}, T^{0}, T^{-} and T^{n0} stand for the photoproduction amplitudes of the reactions (1-1), (1-2), (1-3) and (1-4), respectively. $T^{(0)}$ stands for the isoscalar amplitude which carries only the isospin 1/2, and $T^{(1/2)}$, and $T^{(3/2)}$ are the isospin 1/2 and 3/2 parts of the isovector amplitude, respectively.

In the energy region where resonances having the isospin 1/2 play a dominant role, the isoscalar amplitude $T^{(0)}$ and the isovector amplitude $T^{(1/2)}$ can contribute to the formation of these resonances. In general, it is impossible to separate $T^{(0)}$ and $T^{(1/2)}$ separately by measurements of the photoproduction from protons alone, because the photoproduction amplitudes are reduced to be as follows, neglecting $T^{(3/2)}$, in this energy region;

$$T \text{ (proton)} \propto T^{(0)} + 1/3T^{(1/2)}, \tag{1-9}$$

$$T \text{ (neutron)} \propto T^{(0)} - 1/3T^{(1/2)}. \tag{1-10}$$

Therefore, the experiments on the photoproduction of pions from neutrons are needed to separate $T^{(0)}$ and $T^{(1/2)}$.

On the other hand, the coherent photoproduction of π° mesons on deuterons,

$$\gamma + d \to \pi^{\circ} + d, \tag{1-11}$$

is only induced by the isovector part of the electromagnetic interaction, since the deuteron is an isosinglet. Therefore, an investigation of this process can provide the information on the magnitude of the amplitude $T^{(1/2)}$.

Our previous data of the differential cross section for the reaction (1-11) at the c.m. pion angle of $50 - 60°$ and in the energy range 500-820 MeV indicate that the isovector part is dominant in the D_{13} amplitude of the π° production from nucleons.[5]

In order to clarify the behavior of $T^{(0)}$ and $T^{(1/2)}$ amplitudes in the energy region around the second resonance N' (1520), the differential cross section for the reaction (1-4) was measured at 90° around the energy of 750 MeV. The result of this preliminary experiment supports the dominance of the isovector amplitude.[6]

The measurement on the reaction (1-4) has been performed increasing the momentum and angular resolution of the π° meson and neutron detecting systems and extending the energy region of incident photons.

The present paper reports the experimental results on the ratio,

$$R_{00} = \frac{d\sigma/d\Omega\,(\gamma n \to \pi^{\circ} n)}{d\sigma/d\Omega\,(\gamma p \to \pi^{\circ} p)}, \tag{1-12}$$

at the c.m. pion angle of 60°, 90°, 105°, 120° and 140° in the energy region between 500 and 900 MeV.

The experimental apparatus and the procedures are described in Sec. 2 and 3, respectively.   Sec. 4 describes the procedure of the data reduction.   The experimental results are presented and the discussions are given in brief in Sec. 5.

2. Experimental apparatus

2-a General descriptions

The experimental apparatus is schematically presented in Fig. 1.   In order to determine of the reaction energy of the π° photoproduction from nucleons in deuterium, it is necessary to measure all momenta of the π° meson and the recoiled nucleon, since the target nucleon is moving in deuterium and the energies of the incident photons have the continuous spectra due to the bremsstrahlung.   This was realized in such a way that coincidence measurements on the recoiled nucleons and the emitted π° mesons were made, including the time of flight (TOF) measurement on the recoiled nucleons.   As is shown in the figure, the π° detector consists of a pair of lead glass Cherenkov counters of the total absorption type, each of which was preceded by a lead spark chamber of 12 gaps.   The total thickness of the lead plates amounted to 2 radiation lengths.   The latter was used to determine a position of the shower origin generated in lead and thus to measure the correlation angle between two decay photons from the π° meson.
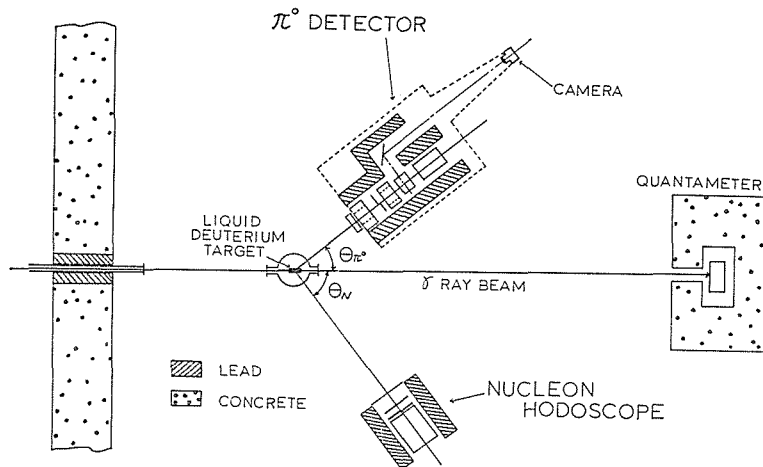

Fig. 1. Schematic diagram of the experimental arrangement.

By the combination of the pulse heights of the Cherenkov counters and the correlation angle, the energy resolution of the π° detector has been greatly improved in comparison with that in the preliminary experiment.

The recoiled nucleon was detected with 16 modules of plastic scintillation counters.   The charge state of the recoiled nucleon was determined by making use of the thin plastic scintillation counters located in front of the nucleon hodoscope.

When coincidences occurred between the π° detector and the nucleon ho-

doscope the spark chambers were triggered and photographed together with the frame number of pictures.   At the same time, all informations from the Cherenkov counters, the nucleon hodoscope and other scintillation counters were recorded in a data processor PDP-5.

Detailed descriptions about the apparatus will be given in the following subsections.

2-b Beam and target

Electrons accelerated by the 1.3 GeV electron synchrotron of Institute for Nuclear Study, University of Tokyo, striked an inner target of Pt $(18.3 \times 10^{-3}$ radiation lengths) and produced the bremsstrahlung beam.   The beam was defined by a lead collimator, which was 30 cm long and 0.5 cm in diameter. The path of the beam to the experimental area was evacuated in order to minimize electron backgrounds from pair productions.   The charged particles were swept away with a sweeping magnet placed behind the collimator.

The beam was incidented upon a liquid deuterium (or hydrogen) target of Wahlin-Reitz type

The container of liquid deuterium or hydrogen, called appendix, was a cir-
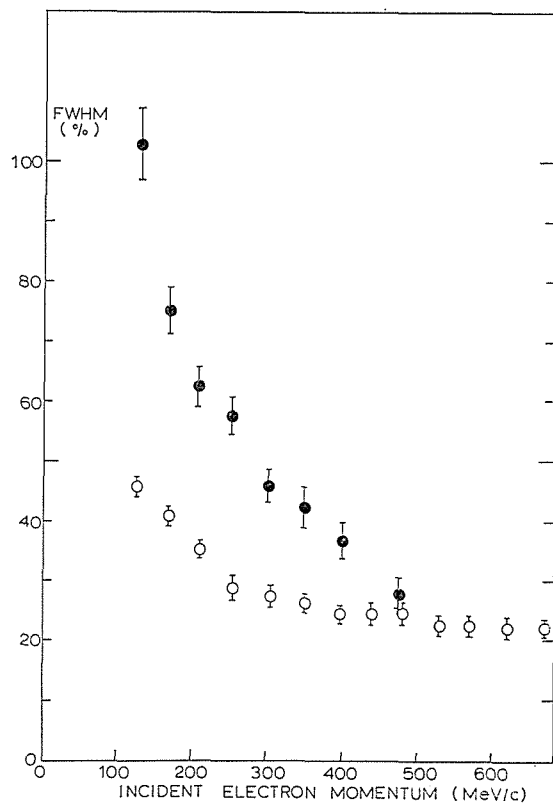

Fig. 2.   Energy resolutions of the Cherenkov counters for the monoenergetic electrons. The points indicated with ● and ○ correspond to the two cases that the lead spark chambers were set in front of the Cherenkov counters and that they were removed, respectively.

cular cylinder of 10.3 cm in length along the beam axis and 5 cm in diameter. This appendix was made of 5 mil mylar, enclosed in a vacuum jacket and surrounded by two concentric 2 mil aluminized mylar for radiation shielding. The vacuum jacket had 10 mil mylar windows. The beam intensity was measured with a Wilson type quantameter.[7]

2-c Cherenkov counter

Two Cherenkov counters used in this experiment detected the photons of the energy range from 100 to 400 MeV decaying from the π° mesons.

The Cherenkov counters were made of SF-2[*] lead glass, the refractive index of which is 1.6477. The shape of the lead glass was a cube ($25\times25\times25$ cm^3) and 9 photomultipliers of RCA6655A's viewed it from the backward side. The mechanical construction of these Cherenkov counters was the same that we had used in the preliminary experiment,[8] except for the optical contact of the photomultipliers was improved.

The gain of these Cherenkov counters were calibrated by using the monochromatic electron beam. Fig. 2 presents the energy resolutions of the incident electrons measured for the two cases that the lead spark chambers were set in front of the Cherenkov counters and that they were removed.

2-d Spark chamber

Each of the lead spark chambers used to detect the two decay photons from the π° meson was consist of 12 parallel plate (thin) chambers. The electrodes of the chamber having a gap of 1 cm were aluminum plates of 0.05 cm in thickness and glued to the Lucite frames. The effective area of these chambers was 25×25 cm^2. Between these chambers, 10 lead plates were placed as converters for photons. The total thickness of the lead converters was 2.0 in radiation length. The chambers were filled with He gas which flowed with a rate of 100 cm^3 per minute. The clearing field was 80 V/cm. The chambers were operated with an applied pulse voltage of 12.5 KV. The spark gap of a high voltage pulser was triggered with the krytron circuit which was drived by a pulse from the counter logic. Under the above operating conditions, the delay time of the pulsing circuit and the sensitive time of the spark chambers were 200 ns and 1 μs, respectively.

The spark chambers were photographed in a stereoscopic way with the use of mirrors and a AUTOMAX camera having the film advance time of 22.5 ms.

2-e π° detector

A side view of the π° detector is shown in Fig. 3. In order to measure the energies and the correlation angle between the two decay photons from π° mesons, each of the Cherenkov counter was preceded by the lead spark chamber, which was described in the preceding subsections. Thus, the energies of the two decay photons from the π° mesons can be measured with a pair of Cherenkov counters. The correlation angles can be determined from the positions of the shower originated in the lead spark chambers. Plastic scintillation counters C1-4 and LiH hardeners, the thickness of which was 0.2 in radiation length, were placed in front of the lead spark chambers to reject charged

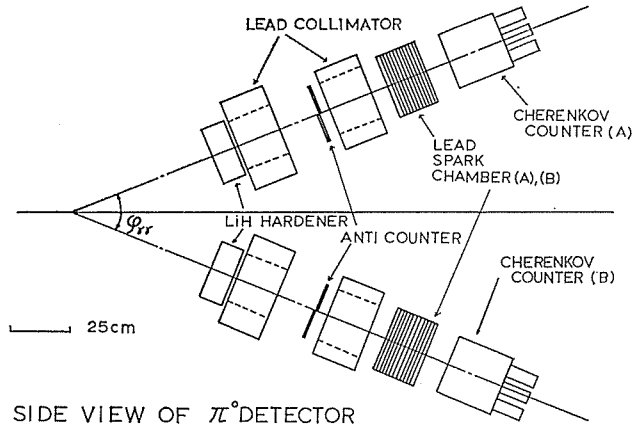*) The lead glass was manufactured by Ohara Optical Glass Co. Ltd., Kanagawa, Japan.

SIDE VIEW OF π°DETECTOR

Fig. 3. Side view of the π° detector.

particles and to absorb low energy photons, respectively. Two lead collimators were also placed in the position which is shown in Fig. 3.

The opening angle of the π° detector was set so as to obtain the maximum detection efficiencies for π° mesons. The momenta of π° mesons were determined as follows; the energies (k_1, k_2) of two decay photons from the π° meson are related to their correlation angle by the energy momentum conservation law,

$$k_1 k_2 = \mu^2/[2(1-\cos\phi)], \tag{2-1}$$

where μ is the pion rest mass.

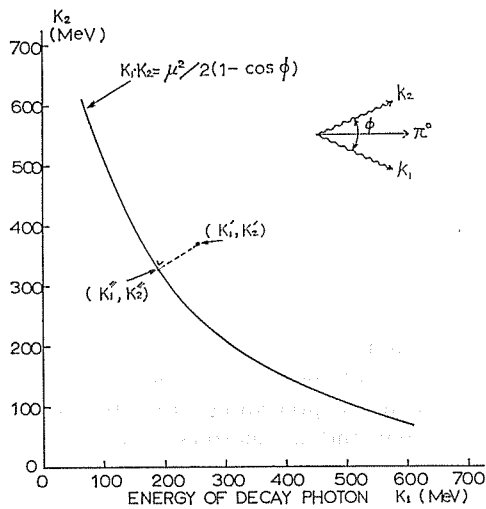If the correlation angle ϕ is precisely determined, the points which repre-

Fig. 4. Determination of the momentum of the π° meson. The most probable decay, photon energies (K_1'', K_2'') can obtained as the point on the hyperbola, $K_1 K_2 = \mu^2/[2(1-\cos\phi)]$, which is at the minimum distance from the point which represents the measured value of the energies (K_1', K_2').

sents the energies (k_1, k_2) should be on the hyperbola (2-1), as is shown in Fig. 4.

The most probable decay photon energies (k_1'', k_2'') can be obtained as the point on the hyperbola, which is at the minimum distance from the point which represents the measured values of energies (k_1', k_2').[9]

Now, the energies (k_1', k_2') were given with the pulse heights of the Cherenkov counters, with the correction for the energy losses of shower electrons in the lead converters calculated by using of the results of Messel et al..[10] From the energies (k_1'', k_2'') and the directions of the two decay photons from the π° meson, the energy and the direction of the π° meson were calculated from the energy momentum conservation law.
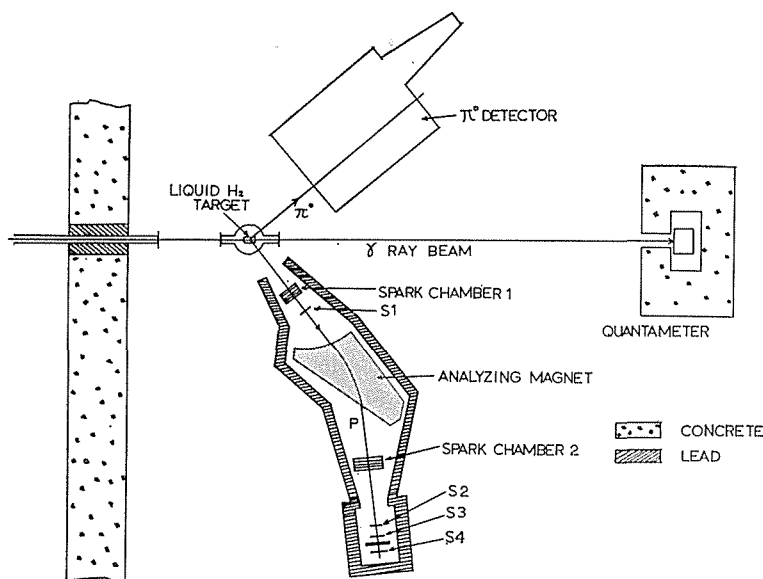

Fig. 5. Schematic diagram of the experimental arrangement for the reaction
$\gamma + p \rightarrow \pi^\circ + p$. S1-4 denote the plastic scintillation counters.

The detection efficiencies, the momentum resolutions and the angular resolutions of the π° detector were measured with the coincidence measurement on the reaction $\gamma + p \rightarrow \pi^\circ + p$ performed by using a liquid hydrogen target at three set-up's. The experimental arrangement is schematically shown in Fig. 5. The recoiled proton was detected by the combination of the momentum analyzing magnet and the time of flight measurement between S_1 and S_2 counters. In order to obtain the more precise informations for the energy and the direction of the recoiled proton, two thin optical spark chambers with four gaps were placed at the position shown in Fig. 5. The measured detection efficiencies of the π° detector were obtained from the following ratio;

$$N(\pi^\circ p)/N(p), \tag{2-2}$$

where $N(p)$ stands for the counting rate of the recoiled proton and $N(\pi^\circ p)$ stands for the coincidence rate between the π° mesons and the recoiled protons. The momentum resolutions and the angular resolutions of the π° detector were obtained by comparing the two values of P_π° and $P_\pi^{\circ\prime}$ for each event, where

Table 1. The measured detection efficiencies, momentum resolutions and angular resolutions of the π° detector. The values calculated by the Monte Carlo simulation are shown in parentheses. P_{π° stands for the averaged momentum of the π° meson; η_{π°, the detection effeciency; $\Delta P_{\pi^\circ}/P_{\pi^\circ}$, the momentum resolution (FWHM); $\Delta\theta_{\pi^\circ}$ and $\Delta\varphi_{\pi^\circ}$, the angular resolutions (FWHM) in the θ and φ directions, respectively.

P_{π° (MeV/c)	η_{π° (%)	$\Delta P_{\pi^\circ}/P_{\pi^\circ}$ (%)	$\Delta\theta_{\pi^\circ}$ (degree)	$\Delta\varphi_{\pi^\circ}$ (degree)
317.9	0.224 ± 0.015	6.0	3.0	8.0
	(0.240 ± 0.012)	(2.9)	(2.3)	(7.5)
502.2	0.393 ± 0.020	7.7	2.8	8.5
	(0.405 ± 0.023)	(2.9)	(2.0)	(5.0)
600.0	0.340 ± 0.039	4.8	2.5	4.8
	(0.378 ± 0.019)	(3.4)	(1.4)	(4.0)

$\boldsymbol{P}_{\pi^\circ}$ stands for the measured momentum vector of the π° meson derived following the above mentioned procedure and $\boldsymbol{P}_{\pi^\circ}{}'$ stands for the momentum vector of the π° meson which was kinematically calculated from the measured momentum vector of the recoiled proton. These measured values are listed in Table 1 together with the results of the Monte Carlo simulations.

From this table, it is seen that the measured detection efficiencies are consistent with the calculated values within the experimental errors.

But, the measured resolutions are somewhat lower than the calculated ones. This fact comes mostly from the accuracy of $\boldsymbol{P}_{\pi^\circ}{}'$ which is estimated to be 3-6 % (FWHM). Consequently, the experimental results show that the momentum resolutions of the π° detector are smaller than 5-7 % (FWHM) for the π° momentum range of 300-700 MeV.

The angular resolutions in the lab. system were also estimated to be $\Delta\theta_{\pi^\circ}$ $\simeq$2-3° and $\Delta\varphi_{\pi^\circ}\simeq$4-8°, where θ_{π° and φ_{π° stand for the azimuthal angle and the polar angle of the π° meson with respect to the direction of the bremsstrahlung, respectively.

2-f   Nucleon hodoscope and counters A1-4

A hodoscope consisting of 16 modules was used to detect the recoiled nucleon, each of which was 10 cm high, 10 cm wide and 20 cm thick, and viewed by a photomultiplier RCA 6655A through a Lucite light guide, as is shown in Fig. 6. They were located in 4×4 matrices symmetrically with respect to the direction of the recoiled nucleons.

In front of this nucleon hodoscope thin plastic scintillation counters A1-4, each of which had the dimension of $0.5\times21\times42$ cm³ and was viewed by a photomultiplier of 56AVP, were placed to identify whether the recoiled nucleon was a proton or a neutron as is shown in Fig. 7. A lead absorber of 0.2 cm (or 0.5 cm) thick was placed in front of these counters to reduce low energy photons. The detection efficiencies of the nucleon hodoscope for neutrons were measured by using the neutron beam which was generated from the reaction $\gamma+p\to\pi^++n$. In order to determine the energy and intensity of neutrons, the π^+ mesons were detected by a similar experimental arrangement as is shown in Fig. 5.
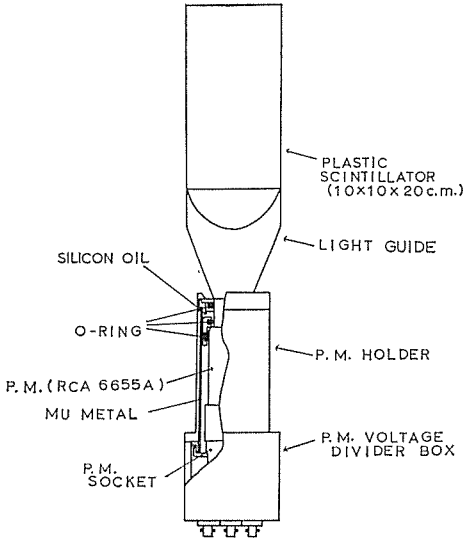
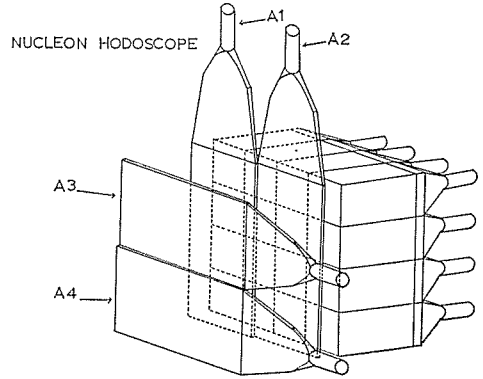Fig. 6. Mechanical construction of one module of the nucleon hodoscope.

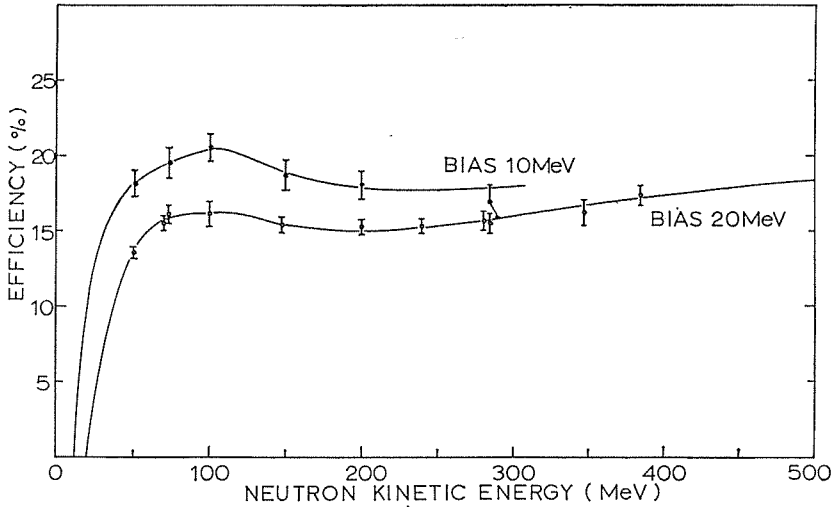Fig. 7. Perspective view of the nucleon hodoscope.

Fig. 8. Detection efficiencies of the nucleon hodoscope for neutrons versus the neutron kinetic energy. The measured values for two cases in which the bias of the nucleon hodoscope was set at 20 MeV and 10 MeV in terms of the proton kinetic energy are indicated with ○ and ●, respectively. Solid curves represent least squares fits to data points with the power-series polynomial for conveniences of computer calculations.

The experimental values obtained are presented in Fig. 8 for the values of two different biases of the electronics. The indicated errors are purely statistical. Solid curves shown in this figure represent least squares fits to data points with the power-series polynomial for conveniences of computer calculations.
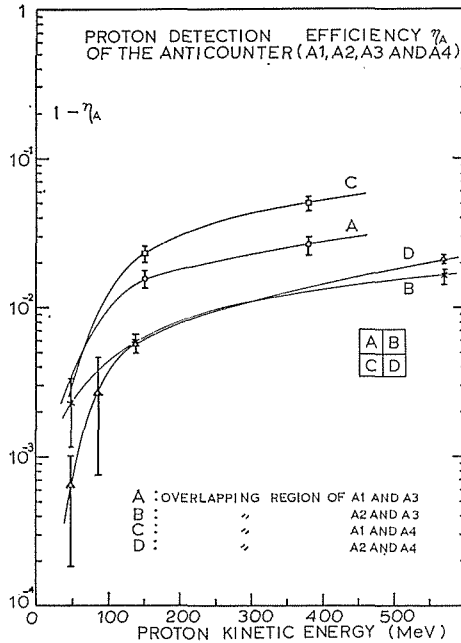
Fig. 9. Detection efficiencies, η_A's, versus the proton kinetic energy for four regions of the A1-4 counter system. In the ordinate the values of $(1.0 - \eta_A)$ are plotted.

Moreover, the detection efficiencies of the counters A1-4 for protons were measured by using protons, momenta of which were analyzed by the magnet. Fig. 9 shows the measured values of the proton detection efficiencies versus the kinetic energies of the protons for the four regions of the A1-4 counter system.

2-g Electronics

The kinetic energy of the recoiled nucleon was evaluated from the TOF measurement on the recoiled nucleons. The time difference between the pulses from the Cherenkov counter and that of the nucleon hodoscope were measured with a time to pulse height converter (TPC). In order to achieve the good time resolution of the TOF measurement, a pulse height compensation device was added to the TPC. Owing to this device, the pulse height dependence of the TOF measurement reduced to be less than 1 ns for the range of the pulse heights used. The time calibration between the Cherenkov counter and one module of the nucleon hodoscope was performed by using a light pulser. The light pulser was also used to adjust the timing between 16 modules within 1 ns.

The block diagram of the electronics is presented in Fig. 10. Main features of the electronics are as follows: the coincidence pulses of a pair of Cherenkov counters were served as the $\pi°$ signals. When the signals from any of 16 modules of the nucleon hodoscope coincided with the $\pi°$ signals, its coincidence signals (called $N\pi°$ signals) were used as the gate pulses for all gated circuits and the trigger pulses for pulsing the spark chambers. The $N\pi°$ events were separated into the $p\pi°$ events from the reaction $r+p\rightarrow\pi°+p$ and the $n\pi°$ events from reaction $r+n\rightarrow\pi°+n$ by the information from the counters A1-4, according
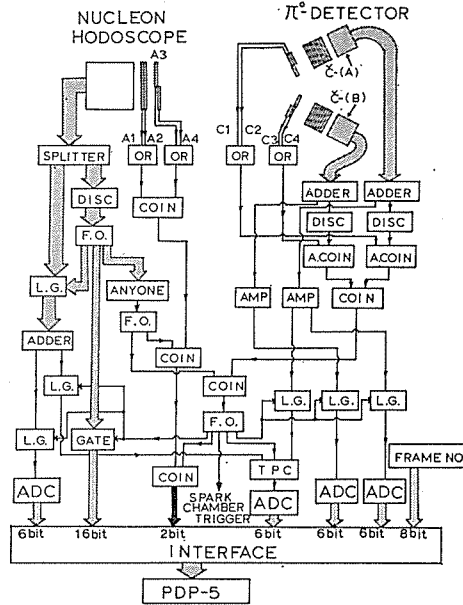
Fig. 10. Block diagram of the electronics. L. G. denotes the linear gate; F. O., the fanout circuit; DISC, the discriminator; COIN, the coincidence circuit; TPC, the time to pulse height converter to which the pulse height compensation device was added; ADC, the analog to digital converter of 64ch (ND160F).

to the scheme as is shown in Fig. 10.

The $N\pi^\circ$ signals also generated interrupt signals to the data processor PDP-5 to allow it to accept the following informations for each event; the pulse heights of the two Cherenkov counters, the time of flight of the recoiled nucleon, the pulse height of the nucleon hodoscope, the labelling of a neutron or a proton for the recoiled nucleon, the address of the nucleon hodoscope struck by the recoiled nucleon, and the frame number of the spark chamber pictures.

A $N\pi^\circ$ event required the 50 bits of the computer storage. As the PDP-5 data processor is not large enough to provide the extensive on-line analysis of the data, the data obtained were perforated on the paper tape.

The checks on the stability of the all photomultipliers and the electronic circuits were made throughout the experiment by monitoring the counting rates of the counters.

For each $N\pi^\circ$ event, the electronic circuits were inhibited their operations for 0.4 s, which was needed to perforate the above informations on the paper tape.

3. Experimental procedure

The experiment was performed in various set-up's to measure the differential cross sections of the reaction $\gamma+n \rightarrow \pi^\circ+n$ in the energy range 500-900 MeV and the angular region 45-140° at the c.m. system. The geometrical parameters of the experiment are listed for each run in Table 2. The first character (D or P) means the use of the liquid deuterium or hydrogen target. For

Table 2. Geometrical parameters of the experiment for each run. $\theta_{\pi}{}^{\circ}$ and θ_N stand for the azimuthal angles of the π° detector and the nucleon hodoscope to the direction of the incident bremsstrahlung, respectively; L_c and L_N , the distances from the center of the target to the forward faces of the Cherenkov counters and the nucleon hososcope, respectively; φ_{rr} , the opening angle of the π° detector.

Run	$\theta_{\pi}{}^{\circ}$ (degree)	θ_N (degree)	L_c (cm)	L_N (cm)	$\varphi_{rr} \cdot 1/2$ (degree)
D-500-100	76.79	37.38	178.80	301.6	22.01
D-600- 60	38.84	57.48	237.84	285.5	14.86
D-550- 90	62.63	44.0	192.03	300.0	18.80
D-600-105	76.79	36.06	176.84	400.0	19.41
D-600-120	92.68	28.91	175.91	399.0	21.63
D-600-140	113.12	20.93	170.35	347.5	24.38
D-750- 45	28.45	63.38	278.54	296.4	11.39
D-750- 60	38.84	55.94	235.34	297.6	12.21
D-750- 90	62.63	41.17	188.36	397.9	14.90
D-750-105	76.79	34.01	173.43	395.2	16.75
D-750-120	92.68	26.97	173.18	400.0	19.03
D-750-140	117.70	17.83	186.43	352.6	22.38
P-600-105	76.79	34.01	176.84	400.0	19.41
P-750-105	76.79	34.01	173.43	386.4	16.75

example, [D-750-90] means that the target used was the liquid deuterium and the π° detector and the nucleon hodoscope were set to fulfill the two body kinematics of the reaction $\gamma + n \to \pi^{\circ} + n$ at the photon energy of 750 MeV in the system in which the target neutron is at rest and the c.m. pion anle of 90°.

During our experiment, the bunch width of the photon beam was kept to be 4 ms as to reduce the rate of the accidental coincidences. The maximum photon energy was taken at 950 MeV for all runs except for a part of the [D-550-90] run.

4. Data reduction

4-a Film scanning

About 200,000 pictures of the lead spark chamber have been scanned and measured by four scanners. During scanning process, the shower events which initiated from the lead converter in the lead spark chamber were selected.

These shower events on the pictures were identified easily except for the case in which spurious sparks or background electrons obscured the showers. There were cases in which two showers were found on a picture. For this case the shower generated by the preceding lead converter was chosen as the true event. The former and latter cases were found to occur at the frequency of 5 % and 2 %, respectively. For the events in which the two decay photons from the π° mesons were converted in the lead spark chambers, the coordinates of the starting points of showers were measured. The spacial accuracy of determining the conversion points was ± 0.3 cm, including the systematic errors due to the difference of the characteristics of the projectors. The average time
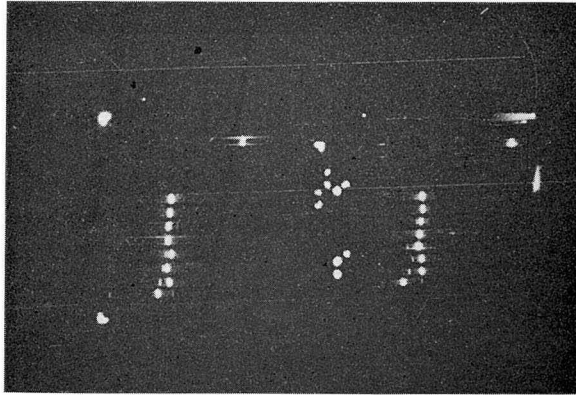
(a)
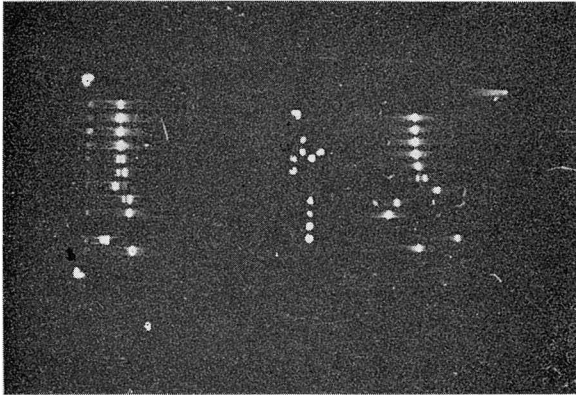
(b)

Fig. 11.   a) Typical example of the shower events in the lead spark chamber.
            b) Typical example of the electron background.

taken to scan and measure one good event was 2.5 minutes. A typical photo-
graph of shower event in the lead spark chambers is shown in Fig. 11.

In order to show that the showers were caused by the high energy photons,
the conversion rate of the photons as a function of the thickness of the lead
converter is presented in Fig. 12. The informations obtained by the film scan-
ning were punched out on a IBM card together with other data for each $2r$'s
converted event.

4–b   Kinematical reconstruction

In order to determine the kinematics of the measured events, the kinematical
reconstruction was performed with a computer FACOM 230–60 for the events
in which the two decay photons from the $\pi°$ mesons were converted in the lead
converters and time of flight of the recoiled nucleon fall within an acceptable
region in the time spectrum. As a typical example, the bidimensional plot
between the neutron time of flight and the pulse height induced in the nucleon
hodoscope by the neutron for the [D–750–105] run is shown in Fig. 13(a).
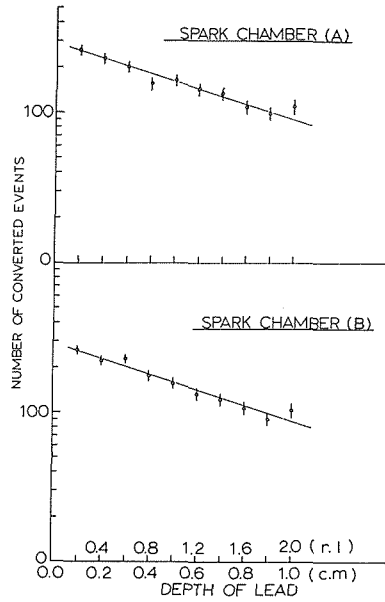Figure 13(b) shows the time spectrum of the corresponding run. Figure 13(a)

Fig. 12.   Conversion rate of the photons as a function of the
          thickness of the lead converter.

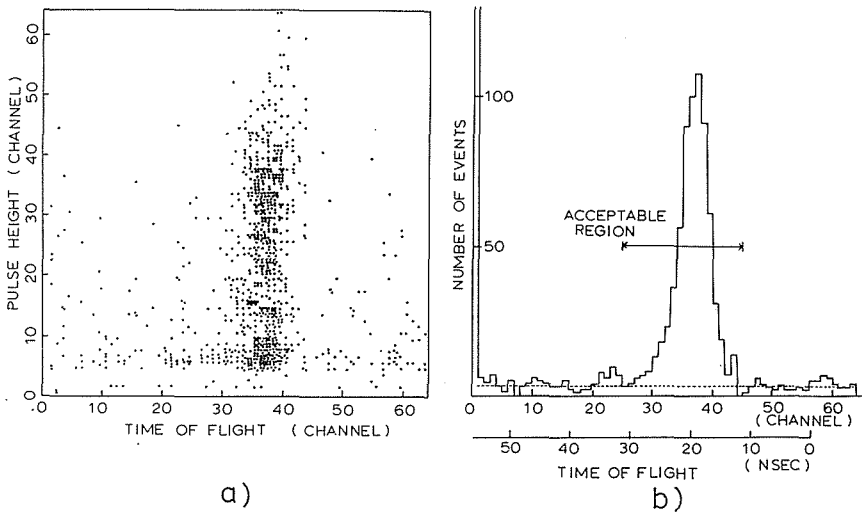a)   b)

Fig. 13.   a) Bidimensional plot between the neutron time of flight and the pulse height
          induced in the nucleon hodoscope by the neutron for the [D-750-105] run.
          b) Spectrum of the neutron time of flight for the same run as in a).

clearly shows that the dependence of the output pulse height from the TPC
circuit on the pulse height of the input pulses becomes to be negligibly small
by use of the compensation device.

For the events, the time of flight of which falls within the acceptable region,
the momentum of the π° mesons were calculated with the procedure as described
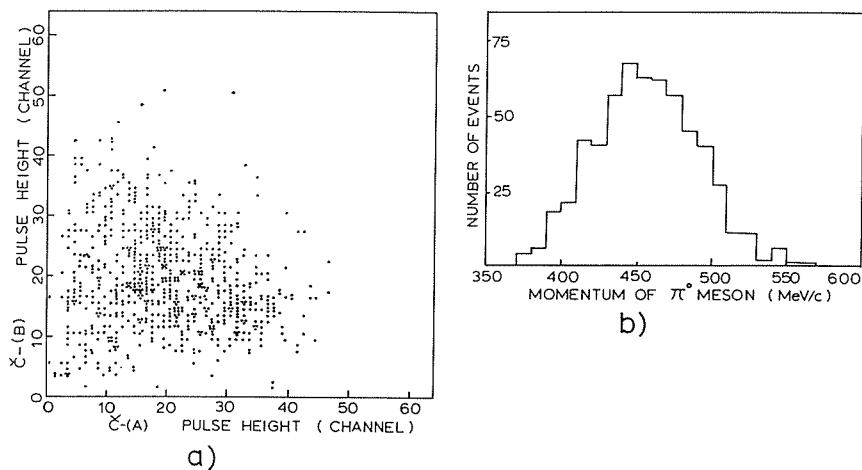
Fig. 14. a) Bidimensional plot between the pulse heights of the two Cherenkov
         counters for the [D-750-105] run.
       b) Momentum distribution obtained from the pulse heights according to
         the procedure described in Sec. 2-e.

in Sec. 2-e. The momentum distribution thus obtained is illustrated in Fig. 14
together with the bidimensional plot between the pulse heights of the two
Cherenkov counters. At the same time, the azimuthal and polar angles of the
π° mesons with respect to the incident bremsstrahlung were calculated to obtain
the momentum vectors of the π° mesons.

The direction of the recoiled nucleon was defined in the following way;
when the single module of the nucleon hodoscope was fired, the nucleon direc-
tion was defined from the center of the forward face of this module and the
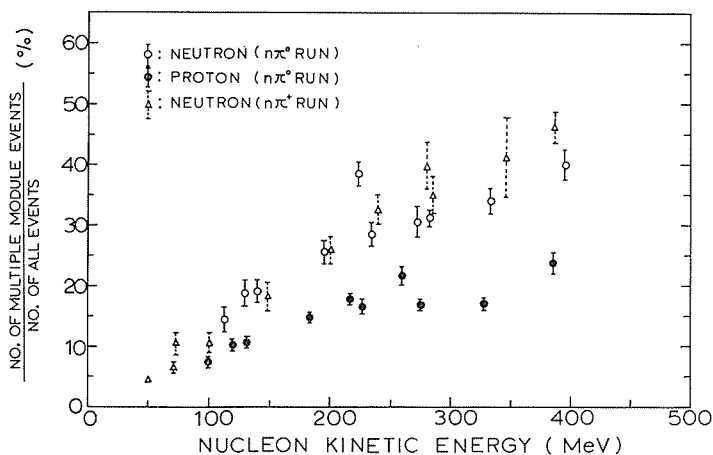

Fig. 15. Ratio of the number of multiple module events to the number of all events
         versus the hinetic energy of the nucleon (proton or neutron). The points in-
         dicated with ○ and ◉ are from the $n\pi^\circ$ events and $p\pi^\circ$ events of the D-runs,
         respectively. The points indicated with △ are from the reaction $\gamma + p \rightarrow \pi^+ + n$
         performed by using a liquid hydrogen target.

center of the target as the incident position on the nucleon hodoscope and the reaction point, respectively.

However, two or more modules which were adjacent were frequently fired. This feature is shown in Fig. 15, where the ratio of the number of multiple module events to the number of all events versus the kinetic energy of the recoiled nucleon is plotted. This ratio for neutrons is inclined to become higher than that for protons as energies increase. The majority of multiple module events was the double module events. Triple or more module events were 7 % of the double ones for the neutrons with the kinetic energy of 400 MeV. For these events, the incident positions of the recoiled nucleons on the nucleon hodoscope were defined as the center of gravity of the forward faces of these adjacent modules. Due to these procedures, the angular resolutions for the recoiled neutrons becomes worse than that for the protons.

The momentum of the recoiled nucleous were determined from the pulse height of the TPC circuit. The time scale corresponding to the pulse height of the TPC output pulses was calibrated by using accurate delay lines. The adjustment to minimize the differences of the time delay between each module of the nucleon hodoscope was made by using a light pulser. However, this adjustment was not accurate enough for our purpose. The data of the P-run with the liquid hydrogen target allows us to estimate these differences more accurately. For the reaction $\gamma + p \rightarrow \pi^\circ + p$, the momentum of the proton in the final state can be determined when the momentum of the π° meson is known and the target proton is at rest. The momentum of the π° mesons were obtained with the procedure described in Sec. 2-e. Then the corresponding proton momentum, consequently the address of the nucleon hodoscope in which the proton was detected and the time of flight of the proton, was calculated. This calculation gives the time distribution of protons for each module of the nucleon hodoscope, which is expected from the measured π° momentum. These expected time distributions were compared with the measured distributions of the P-runs, then the differences of the peak position of the time distribution for each module of the nucleon hodoscope were carefully examined. The average difference for 16 modules was found to be less than 1 ns. These differences for each module were fold into the calculation of the kinematical reconstruction as the corrections.

Finally, for the event obtained in the D-runs, the kinematical quantities in the initial state of the reactions $\gamma + n \rightarrow \pi^\circ + n$ and $\gamma + p \rightarrow \pi^\circ + p$ are deduced from the measured momentum vectors of the π° mesons and the recoiled nucleons in the final state of the reaction.

In order to obtain the event rate of the reaction $\gamma + n \rightarrow \pi^\circ + n$, for each $n\pi^\circ$ event the following efficiencies were considered;

(i) Since some protons were detected as neutrons due to the proton counting losses of the A1-4 counters, each $n\pi^\circ$ event was considered to have the event rate of

$$1.0 - \frac{1.0 - \eta_A}{\eta_A} \cdot \frac{P}{N}, \tag{4-1}$$

where η_A stands for the proton detection efficiency of the A1-4 counters which depends on the kinetic energy of the recoiled proton and the address of the nucleon hodoscope on which the recoiled proton incidented, as is shown in Fig.

9. P and N stand for the normalized counting rates of the $p\pi^\circ$ event and the $n\pi^\circ$ event, respectively.

(ii) The next one is the detection efficiency of the nucleon hodoscope for neutrons. The event rate of each $n\pi^\circ$ event was divided by the efficiency as shown in Fig. 8.

If the recoiled nucleons were protons, they lost their energies due to many materials, such as the liquid deuterium, mylars, the lead absorber, plastic scintillators and air, which were along their flight path. For our experimental arrangements, the corrections for the proton time of flight due to the energy losses were less than 1 ns. Then this correction could be neglected. However, for the [D-750-45] run the average proton kinetic energies were 60 MeV at the reaction point, so that an appreciable amount of protons were lost due to the electronical threshold of the nucleon hodoscope. Therefore, the proton data for this run was not eligible to obtain the $p\pi^\circ$ event rate.

4-c Backgrounds

The backgrounds from the liquid target container was negligibly small and less than 0.2 % of the true event rate. However, the backgrounds due to the accidental coincidences amounted to be 5–25 % for various set-up's by assuming that they are distributed uniformly in the TOF spectrum as is shown by the dotted line in Fig. 13(b). Then, the subtraction of the background of this kind was made in the following way.

Firstly, the distribution of the various kinematical quantities corresponding to these background events were calculated. In Fig. 16, the dotted line represents the distribution of the incident photon energies in the system in which the target nucleon is at rest (called K' distribution) for the [D-750-105] run. The solid line represents the K' distribution of the same run for the good events, the time of flights of which are within the acceptable region.

Consequently, the K' distribution for the true events was obtained by subtracting the dotted one from the solid one.

Once the K' distributions were obtained for both reaction $\gamma + p \rightarrow \pi^\circ + p$ and
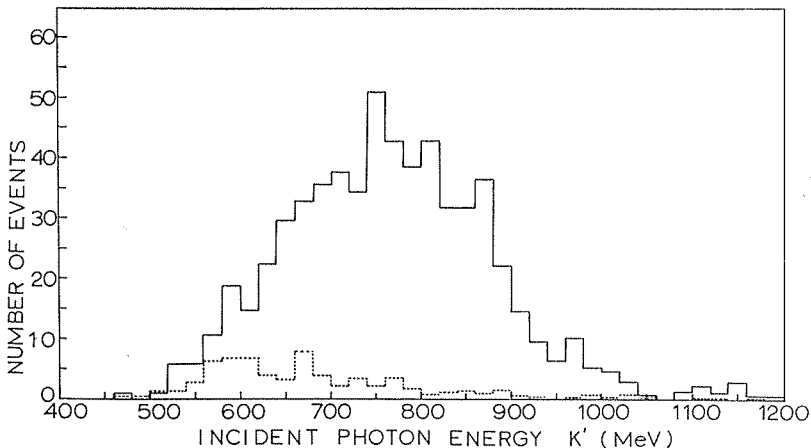

Fig. 16. K' distribution for the $n\pi^\circ$ events of the [D-750-105] run. The dotted line represents the K' distribution for the background events.

$\gamma+n\to\pi°+n$, the experimental values of R_{00}'s were deduced from the following ratio;

$$R_{00} = \frac{d\sigma/d\Omega\,(\gamma n\to\pi°n)}{d\sigma/d\Omega\,(\gamma p\to\pi°p)} = \frac{N_{\pi°n}}{N_{\pi°p}}, \tag{4-2}$$

where $N_{\pi°n}$ and $N_{\pi°p}$ stand for the number of true events for the $\gamma+n\to\pi°+n$ and $\gamma+p\to\pi°+p$, respectively. N's correspond to the area under the histogram in the photon energy interval between two adjacent dotted lines as is shown in Fig. 18. Then, the photon energy interval was 50 MeV, which is comparable to the energy resolution of the whole detecting system of the present experiment.

4-d Monte Carlo simulations

The Monte Carlo simulation was used to evaluate the resolution of the whole detecting system. In this calculation the spectator model and the momentum distribution of target nucleons expected from the Hulthén wave function were assumed.

By comparison between the simulated and reconsctucted quantities the experimental resolutions were deduced. In the case of the [D-750-90] run, for example, the energy resolution was 8 % (FWHM) in K' and the angular resolution was $\pm3.5°$ in $\theta_\pi°^*$, where $\theta_\pi°^*$ stands for the c.m. pion angle.

In Fig. 17, the histogram represents the experimental values on $|P_{ni}|$ which were determined for the $n\pi°$ events and $p\pi°$ events of the [D-750-105] run by the kinematical reconstructions from the measured momentum vectors in the final state, where P_{ni} stands for the momentum vector of the initial nucleon in
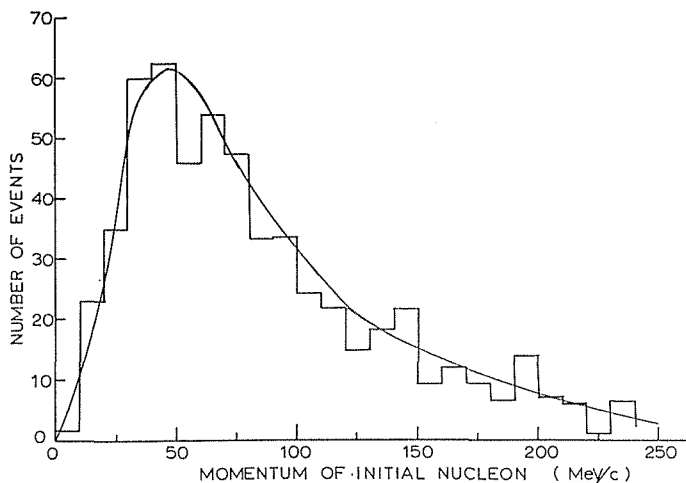

Fig. 17. Momentum distribution of the initial nucleon. The solid curve is obtained from the Monte Carlo simulation.

the lab. system. In Fig. 17, the solid curve represents the result of the Monte Carlo simulation on $|P_{ni}|$, in which the resolutions of the apparatus were folded into.

5. Experimental results and discussions

5-a Experimental results

Table 3. Numbers of pictures taken and pictures scanned.

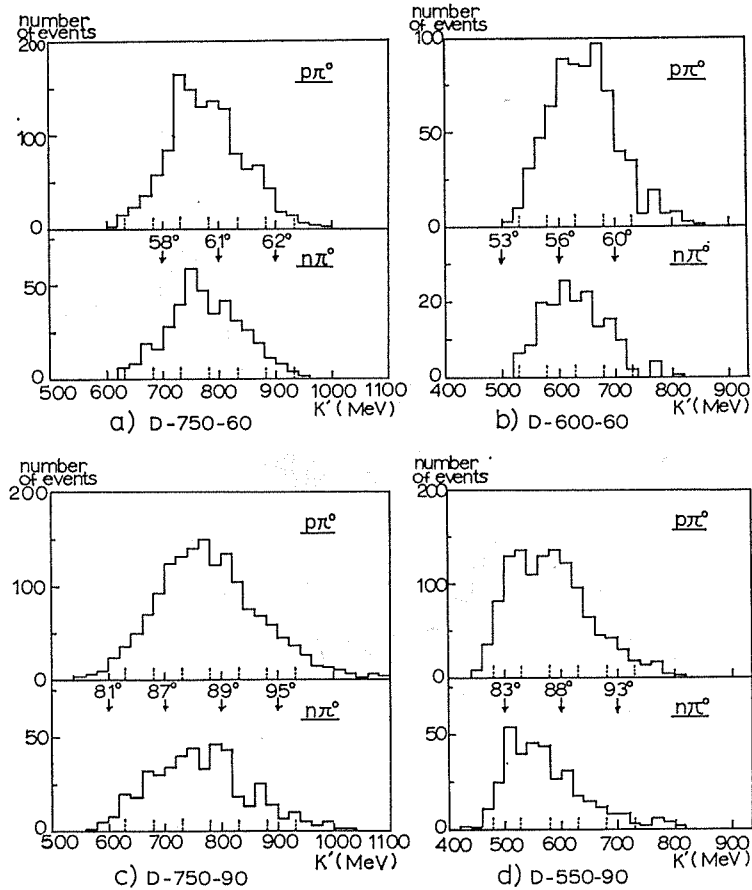| Run	The number of pictures taken (2×10^3)		The number of pictures scanned (2×10^3)		The number of true events	
	$p\pi^\circ$	$n\pi^\circ$	$p\pi^\circ$	$n\pi^\circ$	$p\pi^\circ$	$n\pi^\circ$
D-500-100	4.36	1.56	2.32	1.56	654.8	258.4
D-600- 60	2.12	1.67	2.10	1.63	709.1	175.7
D-550- 90	6.10	2.33	3.19	1.68	1219.3	330.8
D-600-105	5.11	1.66	2.69	1.62	917.0	301.8
D-600-120	5.35	3.04	2.98	3.04	1000.0	325.8
D-600-140	4.64	2.82	3.17	1.97	632.7	168.8
D-750- 45	1.53	1.17	1.44	1.07	585.1	198.5
D-750- 60	5.03	2.51	2.57	2.51	1226.3	402.4
D-750- 90	8.66	3.09	3.09	3.09	1514.1	427.8
D-750-105	11.53	3.49	2.54	3.04	956.4	552.2
D-750-120	7.29	3.29	3.40	3.25	1335.7	448.8
D-750-140	5.27	6.31	4.01	4.81	694.8	177.7

Fig. 18.

The ratios R_{00} have been obtained for 12 runs by the procedure described in Sec. 4.

In Table 3, the numbers of pictures taken and pictures scanned are summarized for each run.

In Fig. 18, the final results of the K' distribution obtained from the true events are summarized for both reactions $\gamma+n\rightarrow\pi^\circ+n$ and $\gamma+p\rightarrow\pi^\circ+p$ at 11 runs except the [D-750-45] run. Since each measurement has been performed at a fixed angle in the lab. system, the corresponding c.m. pion angle $\theta_\pi^{\circ*}$ are indicated in Fig. 18.

Table 4 represents the measured values of the ratio R_{00}, which is the ratio of the area under the histogram of K' for the reaction $\gamma+n\rightarrow\pi^\circ+n$ to that for the reaction $\gamma+p\rightarrow\pi^\circ+p$ in the photon energy interval between two adjacent dotted lines shown in Fig. 18. The ratio obtained from both tails of the histogram of K' was not adopted because of the poor statistics. In Table 4, when the values obtained from different runs belong to the almost same energy K' and c.m. pion angle $\theta_\pi^{\circ*}$, the weighted means of these values are tabulated. The errors quoted are purely statistical; the possible systematic errors are of the order of 5 %. The values in this table are plotted in Fig. 19 for various
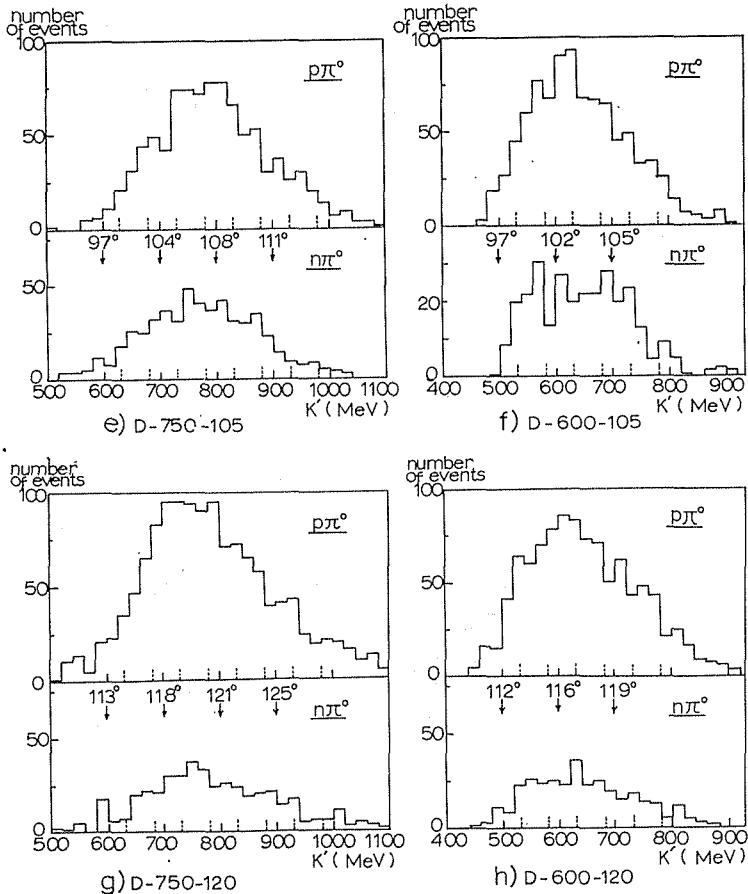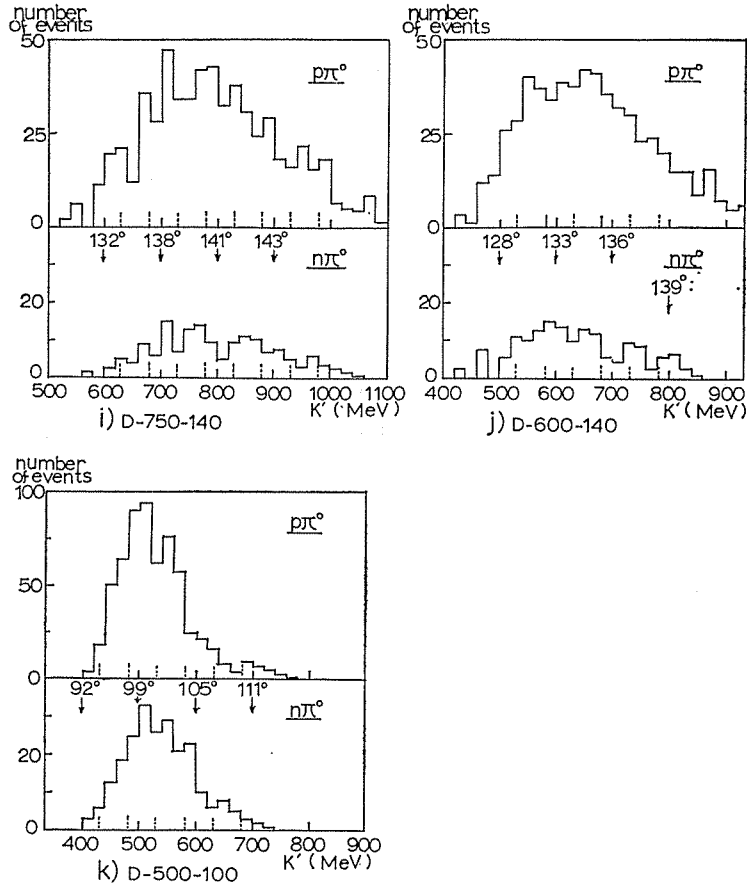

Fig. 18.

Fig. 18. K' distribution for the true events.   The corresponding runs
and c.m. pion angles are indicated in the figures.

Table 4.   Measured values of the ratio $R_{\circ\circ}$.

K' (MeV)	$\theta_\pi^\circ{}^*$ (degree)	$R_{\circ\circ}$
505±25	83.0±3.5	1.45±0.17
	99.0±3.5	1.13±0.16
	112.0±3.5	1.45±0.33
555±25	54.5±3.5	1.27±0.33
	85.5±3.5	1.47±0.16
	101.0±3.5	1.36±0.14
	114.0±3.5	1.93±0.30
	130.5±3.5	1.96±0.41
605±25	56.0±3.5	0.92±0.18
	81.0±3.5	0.93±0.13
	99.5±3.5	0.87±0.12
	116.0±3.5	1.37±0.20
	133.0±3.5	2.20±0.43
655±25	57.5±3.5	1.06±0.14
	87.0±3.5	1.08±0.13
	102.0±3.5	1.13±0.13
	116.5±3.5	1.31±0.15
	134.5±3.5	1.59±0.28

|		
705±25	59.0±3.5	0.88±0.10
	90.0±3.5	0.92±0.11
	104.5±3.5	1.23±0.13
	118.5±3.5	0.01±0.11
	137.5±3.5	1.37±0.30
755±25	60.0±3.5	0.90±0.09
	88.0±3.5	0.85±0.10
	106.0±3.5	0.94±0.10
	120.5±3.5	1.03±0.11
	140.0±3.5	1.56±0.33
805±25	61.0±3.5	0.80±0.10
	89.0±3.5	1.02±0.12
	108.0±3.5	0.80±0.10
	121.0±3.5	0.82±0.12
	140.5±3.5	1.05±0.37
855±25	61.5±3.5	1.05±0.16
	92.0±3.5	0.56±0.09
	109.5±3.5	0.95±0.13
	123.0±3.5	0.83±0.14
	142.0±3.5	1.48±0.35
905±25	62.0±3.5	0.80±0.20
	95.0±3.5	0.71±0.15
	111.0±3.5	0.73±0.14
	125.0±3.5	1.13±0.21
	143.0±3.5	1.48±0.42
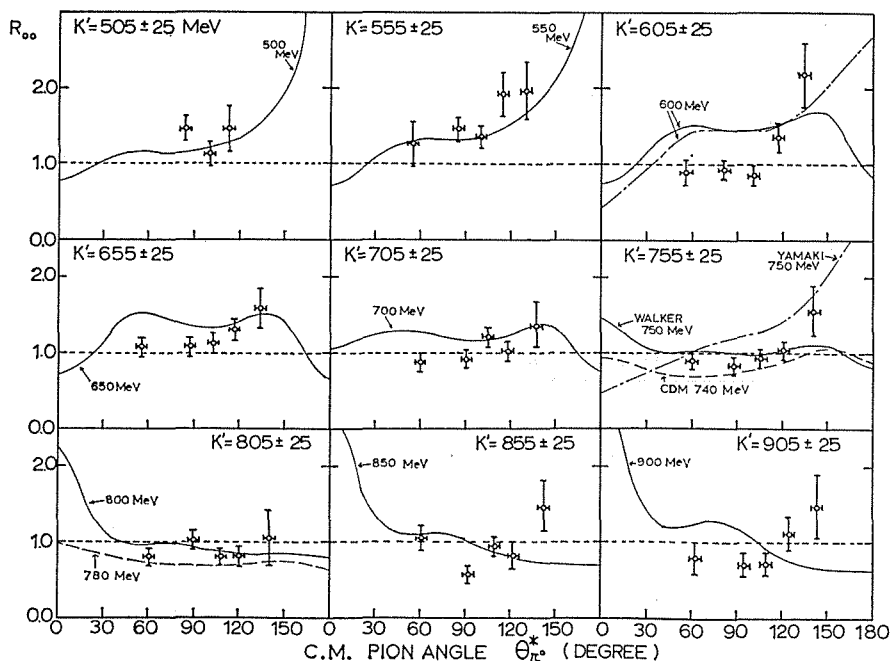
Fig. 19. Angular dependences of the ratio R_{00} in the c.m. pion angle. The Solid, dashed and dot-dashed curves show the calculations by Walker,[11] Chau-Dombey-Moorhouse[12] and Yamaki,[13] respectively. The angular resolution of each point is estimated to be about ±3.5° in the c.m. pion angle.

energies of K' as a function of the c.m. pion angle $\theta_\pi^{\circ *}$.

5-b Discussions

In the energy region of our experiment, Walker[11] and Chau, Dombey and Moorhouse[12] extensively made the phenomenological analyses of the recent pion photoproduction data.   In Fig. 19, their results are plotted together with the analysis by Yamaki.[13]   Yamaki performed the partial wave analysis with the C. G. L. N amplitudes[14] and phenomenological amplitudes.

In the present experiment, main features of the energy dependence of the ratios R_{00} are qualitatively summarized as follows ;

i) The ratios R_{00} at the energy region around the second resonance N' (1520) are nearly equal to unity except at large angles.   This result seem to be consistent with our previous conclusions that the isovector part in the D_{13} amplitude of the pion photoproduction from the nucleon around the second resonance plays a dominant role.[5,6]   However, in order to obtain more precise informations about the ratio of the isoscalar part to the isovector part, the behavior of the non-resonant background amplitude should be taken into account in carrying out the partial wave analysis.

ii) At lower energies (500–600 MeV), there seems to be some trend that the ratios R_{00} become somewhat larger than unity.

It should be noted that in this energy region the effect of P_{11} resonance might be expected to become appreciable, although there is no definite evidence of this kind in the pion photoproduction.   Donnachie suggested that according to the SU_3-symmetry the strong enhancement of the M_{1-} amplitude for the pion photoproduction from the neutron might appear from the constructive interference between the isoscalar and isovector parts.[15]   The results of the present experiment do not indicate such a constructive interference in the M_{1-} amplitude and is interpretable by the S_{11} amplitude (especially by the Born term of this amplitude).   Consequently, the presence of P_{11} resonance is not established by the present results.

REFERENCES

1) Y. Hemmi, T. Inagaki, R. Kikuchi, A. Maki, K. Miyake, T. Nakamura, A. Sasaki, N. Tamura, S. Yasumi and H. Okuno, Phys. Letters 32B, 137 (1970).
2) Aachen-Berlin-Bonn-Hamburg-Heidelberg-München Collaboration, Nucl. Phys. 8B, 535

(1968); P. E. Sheffler and P. L. Walden, Phys. Rev. Letter 24, 952 (1970); E. Lodi Rizzini, G. C. Mantovani, A. Piazzoli, L. Fiore, G. Gialanella, V. Rossi, A. Piazza, G. Rinzivillo, Lett. Nuove Cimento 3, 697 (1970); K. Kondo, T. Nishikawa, T. Suzuki, K. Takikawa, H. Yoshida, Y. Kimura and M. Kobayashi, J. Phys. Soc. Japan 29, 13 (1970); T. Fujii, H. Okuno, S. Orito, H. Sasaki, T. Nozaki, F. Takasaki, K. Takikawa, K. Amako, I. Endo, K. Yoshida, M. Higuchi, M. Sato and Y. Sumi, INS Report 149 (1970), Insiture for Nuclear Study.

3) C. R. Clinesmith, G. L. Hatch and A. V. Tollestrup, Proc. Intern. Symp. on Electron and Photon Interaction at High Energies (Hamburg) vol. II, 245 (1965).

4) K. M. Watson, Phys. Rev. 106, 228 (1954).

5) K. Miyake, K. Baba, S. Hatano, M. Kihara, A. Masaike, T. Nakamura, M. Tamura, T. Yamaki, S. Yasumi and Y. Yoshimura, J. Phys. Soc. Japan 20, 1749 (1965); T. Nakamura, S. Hatano, Y. Hemmi, H. Itoh, M. Kihara, S. Kobayashi, K. Miyake, H. Okuno, T. Yamaki, S. Yasumi and Y. Yoshimura, J. Phys. Soc. Japan 24, 698 (1968).

6) Y. Yoshimura, S. Hatano, Y. Hemmi, R. Kikuchi, S. Kobayashi, K. Miyake, T. Nakamura, H. Okuno and S. Yasumi, J. Phys. Soc. Japan 24, 1395 (1968).

7) T. Miyachi et al., INS-TH-66 (1970), Institute for Nuclear Study.

8) Y. Hemmi, R. Kikuchi, S. Kobayashi, K. Miyake, T. Nakamura, H. Okuno, S. Yasumi and Yoshimura, Nucl. Instr. Methods 56, 213 (1967).

9) L. Tau, Nucl. Instr. Methods 34, 352 (1965).

10) D. F. Crawford and H. Messel, Nucl. Physics 61, 145 (1965).

11) R. L. Walker, Phys. Rev. 182, 1729 (1969).

12) Y. C. Chau, N. Dombey and R. G. Moorhouse, Phys. Rev. 163, 1632 (1967); A. Proia and F. Sebastiani, Lett. Nuovo Cimento 3, 483 (1970).

13) T. Yamaki, Progr. Theor. Phys. 38, 153 (1967).

14) G. F. Chew, M. L. Goldberger, F. E. Low and Y. Nambu, Phys. Rev. 106, 1345 (1957).

15) A. Donnachie, Phys. Letters 24B, 420 (1967).